ORNL/TM-2018/972

Assessment of the Propensity of Low Creep Ductility for Optimized Grade 92 Steel

Lizhen Tan

9/7/2018

Approved for public release.
Distribution is unlimited.

OAK RIDGE NATIONAL LABORATORY
MANAGED BY UT-BATTELLE FOR THE US DEPARTMENT OF ENERGY

ORNL/TM-2018/972

Advanced Reactor Technologies Program
Milestone ID: M3NT-18OR050502052

Assessment of the Propensity of Low Creep Ductility for Optimized Grade 92 Steel

Lizhen Tan
Materials Science and Technology Division

Date Published: 9/7/2018

Prepared by
OAK RIDGE NATIONAL LABORATORY
Oak Ridge, TN 37831-6283
managed by
UT-BATTELLE, LLC
for the
US DEPARTMENT OF ENERGY
under contract DE-AC05-00OR22725

CONTENTS

LIST OF FIGURES

LIST OF TABLES

ACKNOWLEDGMENTS

This research was sponsored by the U.S. Department of Energy (DOE). Programmatic direction was provided by the Advanced Reactor Technologies (ART) Program of the Office of Nuclear Energy (NE).

We gratefully acknowledge the support provided by Alice Caponiti, Director, Office of ART, Sue Lesica, Federal Manager, ART Advanced Materials Program, Robert Hill of Argonne National Laboratory (ANL), National Technical Director, ART Fast Reactors Campaign, and Sam Sham of ANL, ART Technology Area Lead on Advanced Materials.

The author is grateful to Sam Sham of ANL and Hong Wang of Oak Ridge National Laboratory (ORNL) for helpful discussions and overseeing this project, and Jeremy Moser, Tom Geer, and Dorothy Coffey of ORNL for conducting the creep tests, preparing metallographic samples, and preparing FIB-lamellae specimens, respectively. The time spent by Hong Wang and Yanli Wang of ORNL in reviewing this report is also greatly appreciated.

ABSTRACT

A total of twenty-five optimized Grade 92 (Opt.G92) samples were tested at 550, 600, and 650°C in air with stresses ranging from 90 to 280 MPa. Two types of Opt.G92 heats were studied in this work, with one type only fabricated by vacuum induction melting (VIM) and the other type by both VIM and electro-slag remelting (VIM+ESR). All the samples were in the as-received thermomechanical treatment (TMT) condition, except for one sample in the re-normalized and tempered (Re-N&T) condition. Three of the samples are still running, with the longest test time >39,863 h at 550°C. In general, the creep-ruptured samples exhibited consistently superior creep resistance, in terms of longer time to rupture, higher creep strength, and lower minimum creep rate, compared to Grades 92 and 91. For example, Opt.G92 with TMT increased creep strength by ~50 and ~60 MPa with minimum creep rate about two orders of magnitude lower than P92 and P91, respectively, at 550°C. The ongoing test of the Opt.G92 sample in the Re-N&T condition also showed significant enhancement in creep resistance. Although the enhancement in creep resistance of Opt.G92 over P92 and P91 became smaller at higher temperatures, the enhancement is still noticeable at 650°C.

Creep rupture ductility analysis of the available databases of Grades 92 and 91 indicated that creep at higher temperatures tends to have low creep rupture ductility (e.g., reduction of area). Following the trends, Grade 92 is not expected to have reduction of area ≤20% at 550°C unless the stress is <~160 MPa with time to rupture >1,000 kh (or >~114 years), which is way beyond the service life of a nuclear reactor. Grade 91 generally has greater resistance to low creep rupture ductility than Grade 92, in terms of the need of lower stress or longer time to rupture to trigger low creep rupture ductility. Compared to Grade 92 initiated reduction of creep rupture ductility with reduction of area ≤70% at stresses <~100 MPa (or time to rupture >~3 kh) and exhibited low creep rupture ductility with reduction of area ≤20% at stresses <~90 MPa (or time to rupture >~10 kh) at 650°C, Opt.G92 with TMT did not show the initiation of reduction of creep rupture ductility after 16,769.3 h at 650°C and 90 MPa, except for three samples from a VIM-only heat exhibited reduced creep rupture ductility to 30.8–38% reduction of area.

To understand the reason for the normal creep rupture ductility of the samples from the VIM+ESR heats compared to the reduced creep rupture ductility of the samples from the VIM-only heat, microstructural characterization, Vickers hardness measurement, and heat chemistry analysis were conducted. The sample from the VIM-only heat (e.g., #48A2) had reduced creep rupture ductility, associated with dispersed small globular voids in the fracture end with small necking, which is attributable to the creep-induced formation of high-density ultrafine precipitates (~1–6 nm) acting as void nucleation sites and preventing voids coalescence. In contrast, the sample from the VIM+ESR heats (e.g., #64-2 and #41A2) had normal creep rupture ductility, associated with large voids elongated along tensile direction within the large necking region. The creep-induced local microstructure disordering with sizes <1 nm in the samples from the VIM+ESR heats could not influence void nucleation and coalescence. Heats chemistry analyses by a variety of techniques indicated the higher content of tramp elements (e.g., Al, Ca, Ti, Y, Zr, Ag, Pb, Hf, H and D) in the VIM-only heat compared to that in the VIM+ESR heat, which might have favored the ultrafine precipitates as well as volatile phases formation in the VIM-only heat samples.

Further experimental investigations are needed to confirm and clarify the hypothesized mechanisms to understand the overall superior creep resistance, including both creep strength and creep rupture ductility, of VIM+ESR heats of Opt.G92. In summary, Opt.G92 in VIM+ESR heats exhibited significant enhancement in creep resistance with normal creep rupture ductility compared to Grades 92 and 91. Well chemistry and microstructure control can yield excellent performance.

1. INTRODUCTION

For the large-scale industrial deployment of advanced fast reactors, there must be improvements in the capital cost and economic return of such reactors. Further, greater safety margins and increased design flexibility will also be required for any new system. Flexibility, safety, and economics have been identified as key needs for advanced nuclear reactors. Advanced materials play an important role in fulfilling these needs.

The key objective of the advanced materials development sub-activity of the Advanced Reactor Technologies (ART) Program is to develop and qualify advanced structural materials to enable improved reactor performance [1]. Improved structural material performance is one way to improve the economics of fast reactors, by potentially allowing both higher operating temperatures (and thus, higher thermal efficiency and power output) and longer lifetimes for components. Improved materials reliability could also result in reduced down time. Superior structural materials will also spur improvements in high temperature design methodology and thereby allow more flexibility in construction and operation. Advanced materials can have a significant impact on controlling capital construction costs even if the raw materials are more expensive than traditional steels. Advancements in materials performance also enable greater safety margins and more stable performance over a longer lifetime.

Ferritic-martensitic (FM) steels Grade 92 and Grade 92 with special thermomechanical treatments (TMTs) were identified as two of the advanced alloys for further development as part of the ART program [2]. The identified alloys offer considerable improvements in strength and creep resistance over more mature steel, such as Grade 91 (a traditional high temperature material that is used extensively in fossil power plants and selected as a construction material for a number of sodium fast reactor designs), while still maintaining other critical properties at the same levels. The identified alloy Grade 92 had been developed with a variety of compositions. Various tests, including tensile, creep, fatigue, creep-fatigue, Charpy impact, fracture toughness, isothermal aging, weldability, and sodium compatibility, were collaboratively conducted at Oak Ridge National Laboratory (ORNL), Idaho National Laboratory (INL), and Argonne National Laboratory (ANL) in FY 2012 on the developed variants of Grade 92 in small lab scale (<~50 lbs) heats. Based on the overall performance ranking of the test results, optimized Grade 92 (Opt.G92) was down-selected for further development and for intermediate-term testing because of its balanced properties as compared to the other developed variants, e.g., V-modified, Ti-modified, and Ta-modified 9% Cr steels [3]. The exploration of the effects of TMTs on strength and creep resistance led to the selection of two types of TMTs applied to the medium-size (~400 lbs) commercial heats production in FY 2013 and FY 2014, respectively. The basic goal of TMT is to maximize nucleation sites for MX type (M = metal, X = C/N) nanoprecipitates by means of deformation at controlled temperatures or an additional intermediate tempering. An objective of the intermediate term testing was to confirm the observed performance gains based on the small lab scale heat and accelerated tests from FY 2012. The medium-sized heats, produced on a level-of-effort basis at laboratory-scale facility of a commercial steel maker, provided the experience on fabrication, chemistry, and microstructure control of this type of steel.

Intermediate term creep rupture tests of Opt.G92 were initiated in FY 2015 [4]. The progress was updated in FY 2016 [5]. This report summarize the collected and analyzed creep-rupture results of the base metal and microstructural characterization of representative creep-ruptured Opt.G92 samples.

2. CREEP TESTING

2.1 TESTED HEATS

Five heats of optimized Grade 92 with TMT, i.e., 011364 and 011365 procured in FY 2013 and 011441, 011448 and 011449 procured in FY 2014, all from Carpenter Technology Corporation, were tested. The compositions in weight percentage (wt%) and conditions of the heats are summarized in Table 1 and Table 2, respectively.

Table 1. Compositions (wt%) of tested heats of optimized Grade 92 with TMT

Heat/Plate*	C	Cr	Mn	Mo	Nb	Ni	Si	V	W	N	B	Others
64-2	.09	8.74	.36	.36	.06	.12	.01	.19	1.88	.029	.001	<.005P; <.001S; <.01Cu/Al/Ti/Co
65-5	.102	8.84	.4	.36	.1	.11	.06	.21	1.89	.032	.0012	.04Al; <.005P; <.001S; <.01Cu/Ti/Co
41A2	.088	8.73	.34	.36	.03	.15	.02	.16	1.79	.029	.0008	<.005P; .0009S; <.01Cu/Al/Ti/Zr
48A1/A2	.09	8.79	.4	.35	.08	.11	.09	.18	1.79	.051	.0052	<.005P; .0006S; <.01Cu/Al/Ti/Zr
49X2	.089	8.75	.4	.35	.08	.1	.11	.18	1.79	.053	.0045	<.005P; .0007S; <.01Cu/Al/Ti/Zr

* Chemistry were measured from the tested plates of the heats, i.e., the 2nd and 5th plate of heats 011364 and 011365, respectively, with each heat/ingot divided into 5 plates from top to bottom; the 2nd plate from the top section ("A") of heats 011441 and 011448, and the 2nd plate from the bottom section ("X") of heat 011449, with each heat/ingot divided into 4 plates. The locations of the plates from respective heats can be found in Refs. [6,7].

Table 2. Conditions of tested heats of optimized Grade 92 with TMT

Heat	Generic ID	Melting[1]	TMT Processing[2]	Product	Plate IDs
011364	G92-4T	VIM+ ESR	1150°C/1h + HF at 1050°C/WQ + 750°C/1h/AC	301-lb., 1"-thick and 6"-wide plates	#64-2
011365	G92-5T			298-lb., 1"-thick and 6"-wide plates	#65-5
011441	G92-6T		HF from 1130°C + 1130°C/0.5h/WQ + 600°C/1h/AC + 750°C/4h/AC	262-lb., 1.6"-thick and 6"-wide plates	#41A2
011448	G92-8T	VIM		143-lb., 1.6"-thick and 6"-wide plates	#48A1, #48A2
011449	G92-9T			272-lb., 1.6"-thick and 6"-wide plates	#49X2

Notes: [1] VIM – vacuum induction melting; ESR – electro-slag remelting.
[2] HF – Hot forging; WQ – water quench; AC – air-cooling.

The heat compositions suggest major differences between the heats as:

(1) The high aluminum content in #65-5 would consume nitrogen as much as possible due to the formation of AlN as the highest stability of compounds in the alloy system, resulting in the significant reduction of (V,Nb)N type MX precipitates in #65-5 compared to the other heats.
(2) The lower niobium content in #41A2 as a result of ESR limits the amount of (V,Nb)N precipitates.
(3) The well-controlled target compositions in #48A2 and #49X2 with higher nitrogen and niobium contents and lower tungsten favor a higher fraction of MX and a slightly less amount of Laves phase compared to the other heats.
(4) The two TMTs led to different microstructures, i.e., intermediate forging after normalization favored dynamic precipitation of MX in heats 011364 and 011365, while two-step tempering favored both MX and $M_{23}C_6$ precipitations in heats 011441, 011448, and 011449.

2.2 SAMPLES

Standard round bar specimens with a 1/4” diameter gauge section, as specified in Fig. 1, were extracted from the plate-center of the plates, with one specimen per 1”-thick (#64-2 and #65-5) and two specimens per 1.6”-thick (#41A2, #48A1, #48A2, and #49X2) plates. The length direction of the specimens is parallel to the longitudinal direction of the plates.

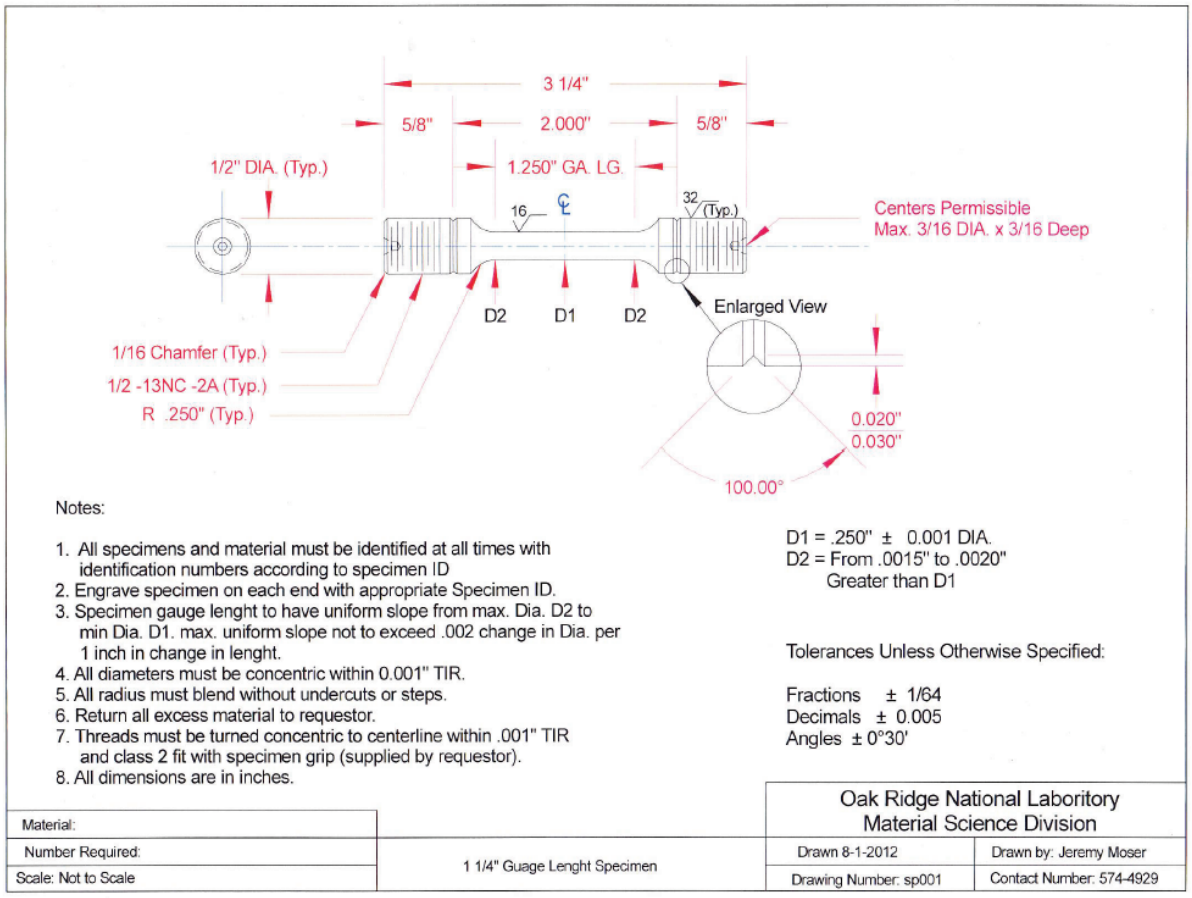

Fig. 1. Specification of creep specimen with a ¼” diameter gauge section.

3. CREEP PERFORMANCE

3.1 TEST RESULTS

Creep tests were conducted at 550, 600, and 650°C, following the ASTM Standard E139-11, "Standard test methods for conducting creep, creep-rupture, and stress-rupture tests of metallic materials". The tested specimens were usually necked and ruptured slightly deviated from the center of the gauge section of the specimens. The creep curves of the ruptured specimens were mostly reported in Ref. [4]. Table 3 lists the creep rupture results for a total of 25 specimens, with 21 of them tested at ORNL (3 of them are still running) and 4 of them tested at INL.

Table 3. Creep rupture test results of optimized Grade 92.

Specimen ID	Test ID	Stress (MPa)	T (°C)	Life (h)	Elongation (%)	Reduction of Area (%)	Minimum creep rate (%/h)	Post test check
64-2-01	TN32194	280	550	1024.9	23.5	79.4	3.67×10^{-3}	✓
64-2-02	TN32195	220	600	474.5	23.9	85.8	7.92×10^{-3}	✓
64-2-03	TN32196	140	650	742.7	24.4	86.4	3.89×10^{-3}	✓
64-2-04	TN32243	200	600	1210.5	23.1	84.3	3.11×10^{-3}	✓
64-2-05	TN32242	130	650	344.8	25.4	86.1	1.07×10^{-2}	✓
64-2-06	TN32244	260	550	4411.9	20.4	76.6	1.04×10^{-3}	✓
64-2-07	TN32250	110	650	3341.2	22.8	78.3	1.41×10^{-3}	✓
64-2-08	TN32260	230	550	>39863				
64-2-09	TN32261	180	600	4902.9	21.0	83.8	8.93×10^{-4}	✓
64-2-10	TN32262	120	650	1950.5	25.5	84.5	1.65×10^{-3}	✓
64-2-11	TN32330	90	650	10815.3	18.8	82.2	4.74×10^{-4}	✓
65-5-01	TN32346	100	650	4147.5	24.6	78.1	9.44×10^{-4}	✓
41A2-4	TN32345	90	650	15864	20.7	86.9	1.44×10^{-4}	✓
48A2-4	TN32344	90	650	19700.2	13.4	38	2.63×10^{-4}	✓
41A2-5	TN32342	90	650	16769.3	23.6	81	3.21×10^{-4}	✓
48A2-5	TN32343	90	650	24229.5	21.4	30.8	1.98×10^{-4}	✓
48A2-26	TN32352	90	650	23143.8	15.9	36.8	2.54×10^{-4}	✓
48A2-12	TN32354	190	600	4282	13	72.1	3.51×10^{-4}	✓
48A2-23	TN32532	270	550	7606.5	21.6	78.5	4.45×10^{-4}	✓
48A2-24	TN32416	260	550	>28988				
49NT01*	TN32533	230	550	>22246				
48A1R-1	INL	280	550	182.1	22.6			
48A1R-2		190	600	1304.1	25.7			
48A1R-3		270	550	440.5	15.8			
48A1R-4		200	600	652.7	17.0			

* NT: Re-normalized and tempered (Re-N&T) at 1130°C/0.5h/WQ + 750°C/2h/AC

3.2 CREEP RESISTANCE

The creep stress is plotted as a function of time to rupture of the tested samples in Fig. 2 for both the 22 ruptured and 3 running specimens. The data of optimized Grade 92 (Opt.G92) are denoted with filled diamonds, which are compared with that of P92 in open triangles (Fig. 2a) and P91 in open circles (Fig. 2b)

at 550 (black), 600 (blue), and 650°C (red). The data of P92 and P91 are extracted from the NIMS Creep Data Sheet No. 48A and No. 43A, respectively [8,9]. The INL-tested four specimens (from #48A1) are shown in shaded diamonds. The ongoing tests of the 3-specimen data are attached with arrows, all at 550°C (one from #64-2, one from #48A2, and one from #49X2). The longest testing time at each temperature has achieved >39,863 h (ongoing) at 550°C and 230 MPa, 4,902.9 h at 600°C and 180 MPa, and 24,229.5 h at 650°C and 90 MPa by the time of this report. Similarly, the minimum creep rate as a function of stress of the Opt.G92 samples are plotted in Fig. 3, which are compared with the literature data of P92 and P91 from the NIMS Creep Data Sheet [8,9]. The slopes of the stress-dependent miminum creep rate relationship of Opt.G92 are approximately the same as P92 and P91 at the three test temperatures, indicating the similar creep mechanisms of the steels.

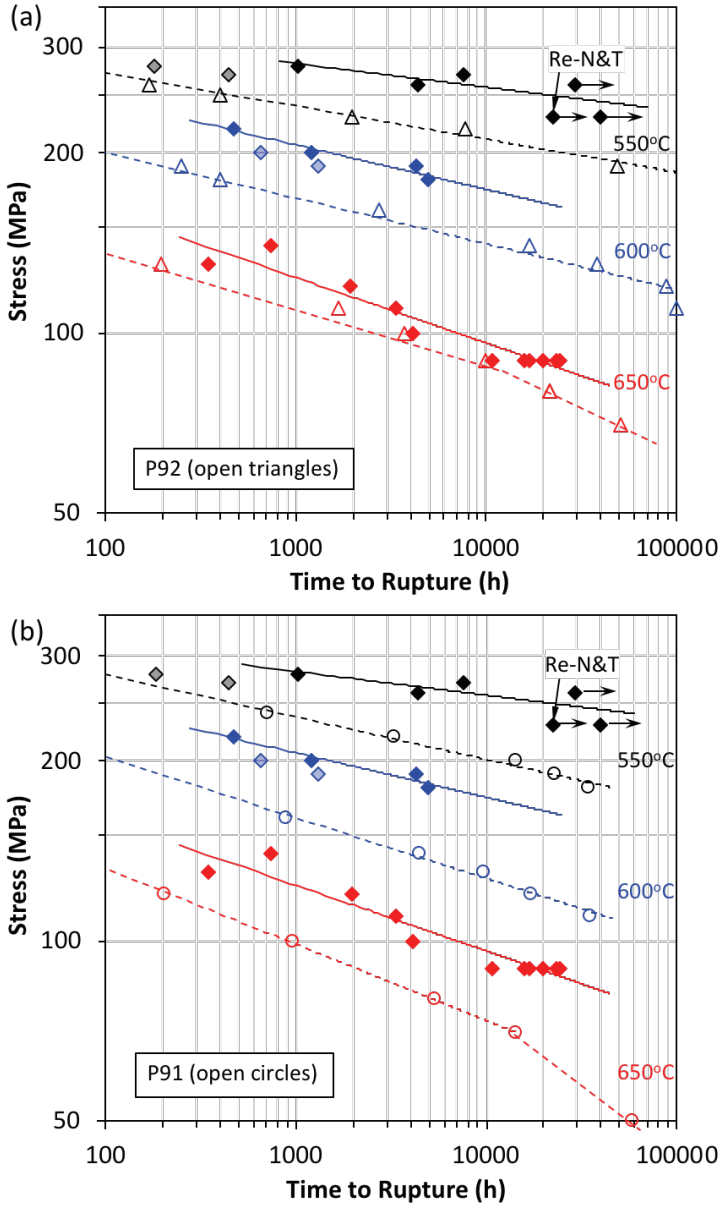

Fig. 2. Stress as a function of time to rupture of optimized Grade 92 compared with (a) P92 and (b) P91 from the NIMS Creep Data Sheet [8,9].

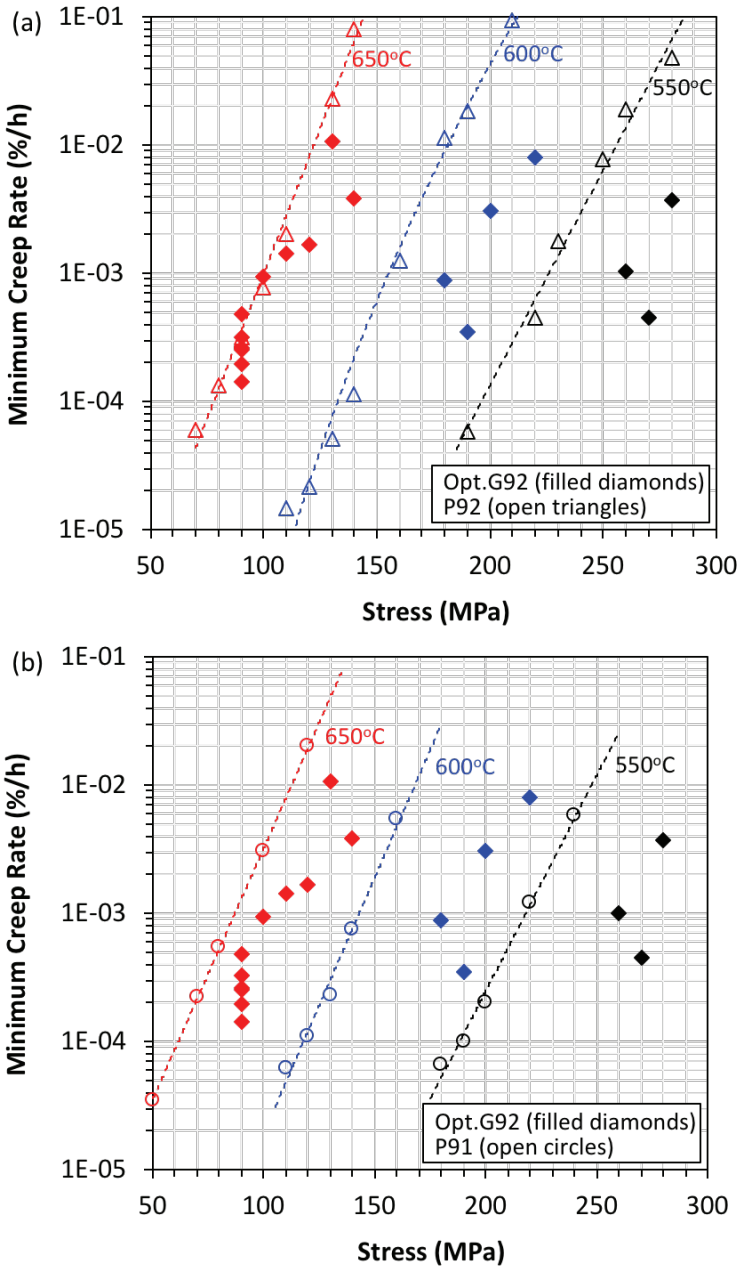

Fig. 3. Stress as a function of time to rupture of optimized Grade 92 compared with (a) P92 and (b) P91 from the NIMS Creep Data Sheet [8,9].

Comparing to P92 and P91, the Opt.G92 exhibited noticeable enhancement in creep resistance in terms of longer time to rupture and higher creep strengths as shown in Fig. 2 and lower minimum creep rates as shown in Fig. 3. The estimated enhancements of Opt.G92 over P92 and P91 based on the available data are summarized in Table 3. Opt.G92 had pronounced advantages over P92 and P91 in creep resistance at 550°C, e.g., ~60 times of the creep life, ~50-60 MPa increases in creep strength, and ~3-4% of the minimum creep

rate of P92 and P91. Although such advantages diminish at higher temperatures, the advantages are still noticeable at 650°C.

Table 4. Creep resistance advantages of optimized Grade 92 over P92 and P91.

T (°C)	Opt.G92 over P92			Opt.G92 over P91		
	Time to rupture ratio [a]	Increased creep strength (MPa) [b]	Minimum creep rate ratio [a]	Time to rupture ratio [a]	Increased creep strength (MPa) [b]	Minimum creep rate ratio [a]
550	~60	~50	~0.04	~60	~60	~0.03
600	~10	~30	~0.08	~30	~50	~0.02
650	~2	~10	~0.7	~9	~25	~0.3

[a] Referring to the time to rupture or minimum creep rate at 250 MPa at 550°C, 160 MPa at 600°C, and 80 MPa at 650°C.

[b] Referring to the increased creep strength at 20,000 h time to rupture.

3.3 CREEP RUPTURE DUCTILITY

Creep rupture ductility of FM steels decreases at higher testing temperatures and longer creep lives (or lower creep stresses). Low creep rupture ductility failure has been reported for Grades 92 and 91 steels tested at temperatures above ~600°C [10].

Fig. 4 shows creep rupture ductility (reduction of area) as a function of stress or time to rupture from the literature data of Grade 92, including P92 (MJP) and T92 (MJT) reported in the NIMS Creep Data Sheet No. 48A [8] and four heats of P/T92 reported in Refs. [11,12,13]. The data show clear relationships between reduction of area and stress or time to rupture as highlighted by the shaded thick lines for the data at each temperature. In general, creep rupture ductility linearly decreases with decreasing stress or time to rupture when the stress is lower or time to rupture is longer than a critical threshold at each temperature. P92 had higher creep rupture ductility than T92 tested at the same stress or time to rupture.

Following the same plot in Fig. 4, the data of Grade 91 are plotted in Fig. 5, including P91 and T91 reported in the NIMS Creep Data Sheet No. 43A [9], together with other forms of products such as plates (1/2"–8" thick), bars, and forging products reported in an ASME report by Swindeman et al. [14]. The data from Ref. [14] were tested at 593 and 649°C, which are grouped with the NIMS Creep Data into the 600 and 650°C data, respectively. The larger database and variety of product forms of Grade 91 resulted in a larger scatter of the data than Grade 92 data in Fig. 4. The relationships between reduction of area and stress or time to rupture of the Grade 91 data in Fig. 5 are not as pronounced as that of the Grade 92 data in Fig. 4. However, the approximate relationships are still perceptible at 600 and 650°C. Simiar to the Grade 92 data, creep rupture ductility decreases with decreasing stress at the test temperatures. However, the relationships between rupture ductility and time to rupture of Grade 91 are not as "simple" as that of Grade 92. Unlike the consistent temperature dependence (i.e., parellel relationship between the temperatures), the relationship between creep rupture ductity and time to rupture at 600°C is mixed with or crosses over the relationship at 650°C. Tests at <~75 MPa and 650°C showed low creep rupture ductility, e.g., 13% reduction of area. Simple extrapolation on low creep rupture ductility at 550°C is not available for Grade 91 from the database. However, the ECCC WG3A data of Grade 91 steel at 550°C showed noticeable decreases in reduction of area to ~20% after ~3,000 h [10]. It indicates the presence of significant Grade 91 heats variations between European and Japan/U.S.

The arrow-pointed three samples in Fig. 4 and Fig. 5, i.e., 64-2-11, 41A2-5 and 48A2-4, are selected for microstructural characterization to discern difference between the normal creep rupture ductility (64-2-11 and 41A2-5) and reduced creep rupture ductility (48A2-4).

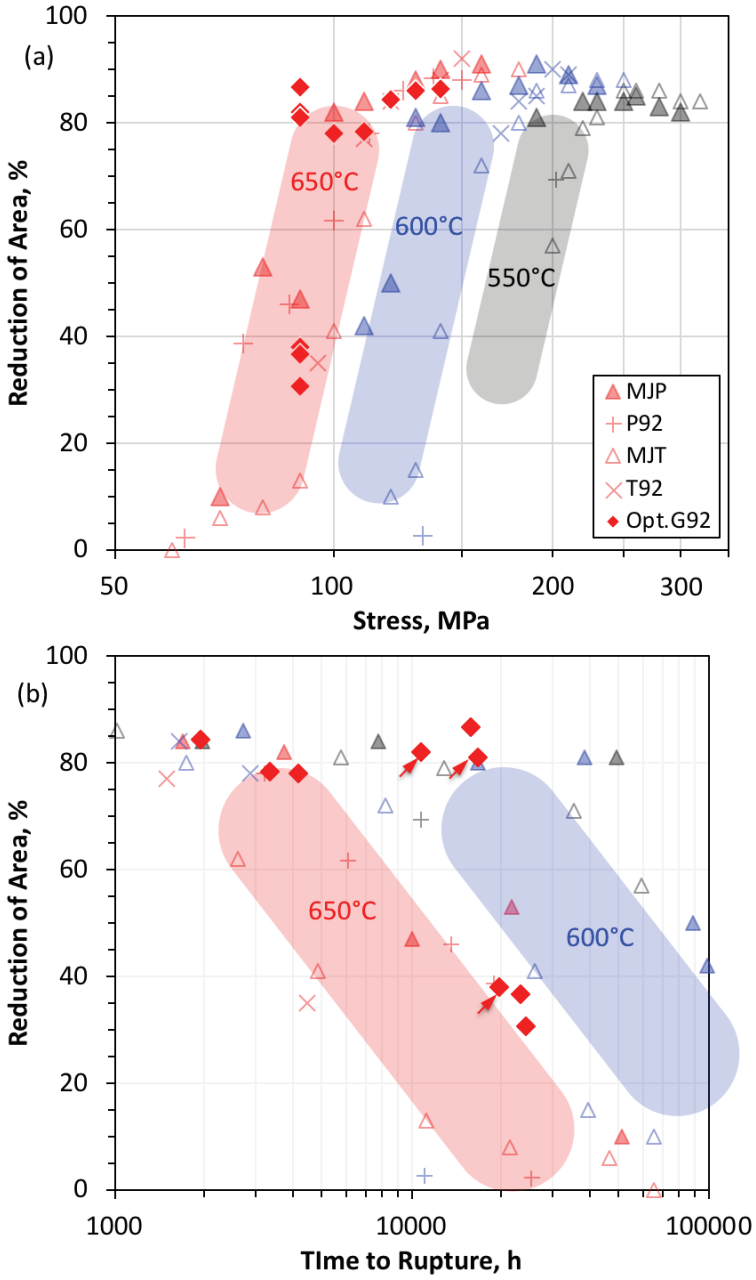

Fig. 4. (a) Stress- and (b) time-to-rupture-dependent reduction of area of optimized Grade 92 compared with P92 and T92 [8,11,12,13].

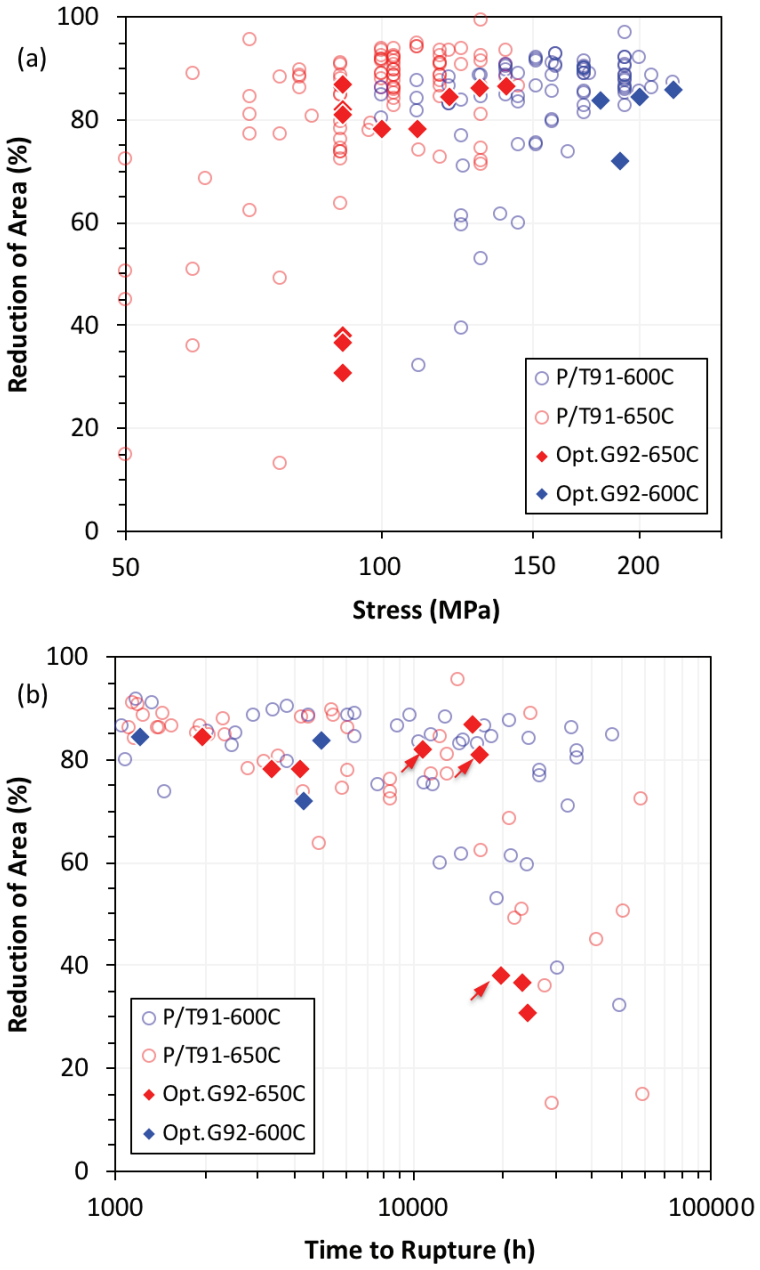

Fig. 5. (a) Stress- and (b) time-to-rupture-dependent reduction of area of optimized Grade 92 compared with P/T91 [9,14].

Table 5 summarizes the initial reduction and low creep rupture ductility of Opt.G92 compared with that of Grades 92 and 91 based on the analyses of Fig. 4 and Fig. 5. Grade 92 at 550°C and <~160 MPa would result in <20% reduction of area, which would correspond to a creep rupture life of >~1×10^6 h (or >~114 years) assuming no change in creep mechanisms after the initial reduction of creep rupture ductility. Such a long time (>~114 years) at 550°C is way beyond the service life of a nuclear reactor. The low creep rupture ductility of Grade 92 becomes pronounced at higher temperatures, e.g., <~110 MPa (or >~40,000 h) at 600°C and <~90 MPa (or >~10,000 h) at 650°C, which suggests that Grade 92 is not safe for use at 600°C and above because of its short creep rupture life with low creep rupture ductility. In contrast, Grade

91 significantly postpones its low creep rupture ductility behavior to <~80 MPa (or >~400,000 h or >~45.7 years) at 600°C and <~50 MPa (or >~50,000 h), suggesting the unsafe use of Grade 91 at temperatures above 600°C. In comparison, Opt.G92 did not show initial reduction of creep rupture ductility for the tests as presented in Table 3. However, three samples from the VIM-only heat (#48) did show creep rupture ductility reduced to 30.8–38% reduction of area at 650°C and 90 MPa, which are in contrast to the VIM+ESR heats (#64 and #41) showing normal reduction of area of 81–86.9% at the same test condition. Unlike Grade 92 exhibited initiation of reduced creep rupture ductility at <~100 MPa and 650°C, the VIM+ESR heats of Opt.G92 did not show initiation of reduced creep rupture ductility even at 90 MPa and 650°C. The analysis for the cause of the VIM heat on reduced creep rupture ductility is presented in Sections 4-5.

Table 5. Initial reduction and low creep rupture ductility of optimized Grade 92 compared with that of Grades 92 and 91.

T (°C)	Opt.G92		Grade 92		Grade 91	
	Initial reduction of creep rupture ductility [a]	Low creep rupture ductility [b]	Initial reduction of creep rupture ductility [a]	Low creep rupture ductility [b]	Initial reduction of creep rupture ductility [a]	Low creep rupture ductility [b]
550	NI [c]	NI	<~200 MPa or >~40 kh	<~160 MPa or >~1,000 kh [d]	NA [e]	NA
600	NI	NI	<~150 MPa or >~20 kh	<~110 MPa or >~40 kh	<~140 MPa or >~15 kh	<~80 MPa or >~400 kh [d]
650	NI	NI [f]	<~100 MPa or >~3 kh	<~90 MPa or >~10 kh	<~70 MPa or >~20 kh	<~50 MPa or >~50 kh

[a] Reduction of area ≤ 70% (used in this work);
[b] Reduction of area ≤ 20% (used in this work);
[c] NI: Not identified in the current work because of the limited test times;
[d] Assuming no change in creep mechanisms at after the initial reduction of creep rupture ductility;
[e] NA: Not available because the database does not show initial reduction of creep rupture ductility although the ECCC WG3A data exhibited reduced creep rupture ductility to ~20% reduction of area after ~3,000 h [10];
[f] Only the heat (#48) fabricated solely by VIM exhibited reduced creep rupture ductility, while the VIM+ESR heats did not show initial reduction of creep rupture ductility.

4. MICROSTRUCTURE OF CREEP-RUPTURED SAMPLES

One of the broken pieces of the creep-ruptured samples of 64-2-11, 41A2-5, and 48A2-4 was sliced along the axial direction using wire electro-discharge machine. The 64-2-11 and 41A2-5 had normal creep rupture ductility (≥81% reduction of area) while 48A2-4 had reduced creep rupture ductility (38% reduction of area) after the same creep condition of 650°C and 90 MPa. The sliced piece from each sample was mounted into epoxy followed by conventional metallographic sample preparation for optical microscopy and scanning electron microscopy (SEM). Focused-ion beam (FIB) was employed to lift-out lamellae from the tab and gauge sections of the polished metallographic samples and then thinned to electron transparent following stepped procedures to reduce artificial FIB damage for transmission electron microscopy (TEM) in both scanning transmission microscopy (STEM) and conventional high-resolution TEM, together with selected area electron diffraction. Energy dispersive x-ray spectroscopy (EDS) was used for chemistry analysis.

4.1 OPTICAL MICROSCOPY

Fig. 6 shows the optical micrographs of (a-d) 64-2-11, (e-h) 41A2-5, and (i-l) 48A2-4 at the tab, gauge, and necking regions. The (a, e, i) tab region of the three samples exhibits a similar microstructure. In contrast, the (b, f, j) gauge region indicates that (j) 48A2-4 tended to have refined grains compared to (b) 64-2-11 and (f) 41A2-5 retaining microstructures comparable to their tab region. The difference between samples with the normal and reduced creep rupture ductility becomes more distinct at the necking region. The necking region of (c-d) 64-2-11 and (g-h) 41A2-5 with normal creep rupture ductility shows noticeable “flowing” (or elongated) microstructure, together with elongated voids, along the tensile (horizontal) direction. However, the necking region of (k-l) 48A2-4 with reduced creep rupture ductility exhibits little “flowing” (or elongated) microstructure, together with globular voids, without obvious orientation relationship with the tensile (horizontal) direction. The voids in the necking region of (l) 48A2-4 are much smaller with a significantly higher density than that in the necking region of (d) 64-2-11 and (h) 41A2-5.

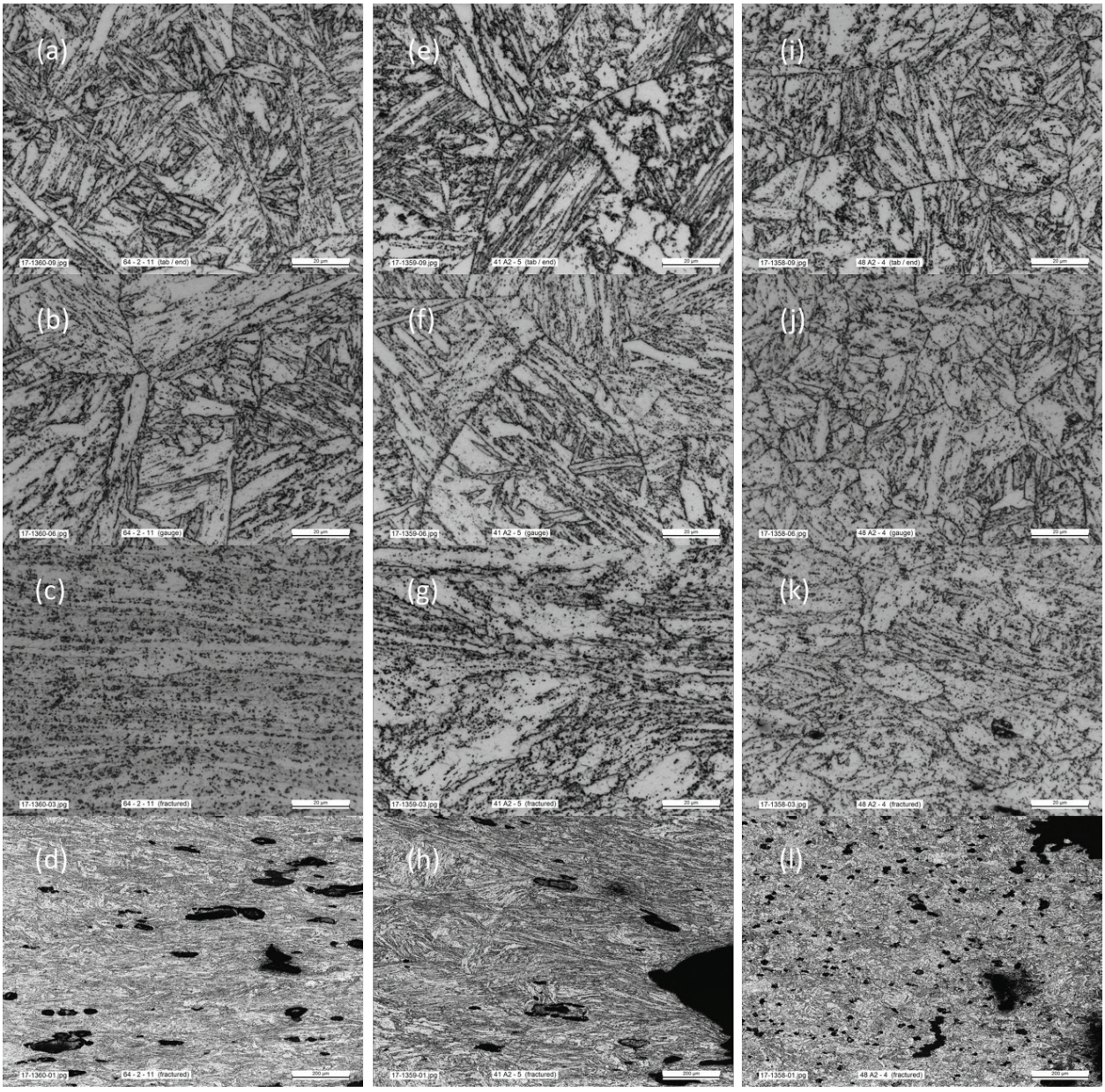

Fig. 6. Optical micrographs of creep-ruptured samples (a-d) 64-2-11, (e-h) 41A2-5, and (i-l) 48A2-4 tested at 650°C and 90 MPa, which were taken from the (a, e, i) tab, (b, f, j) gauge, and (c, d, g, h, k, l) necking regions.

4.2 SEM AND EDS

Fig. 7 shows the secondary electron images of the fracture end of (a) 64-2-11, (b) 41A2-5, and (c) 48A2-4, which revealed significant necking of 64-2-11 and 41A2-5 with normal creep rupture ductility but small (or negligible) necking of 48A2-4 with reduced creep rupture ductility. The elongated voids, usually in large sizes, tended to concentrate at the center of the samples of 64-2-11 and 41A2-5. In contrast, the generally small globular voids are approximately uniformly dispersed in the necking region of 48A2-4.

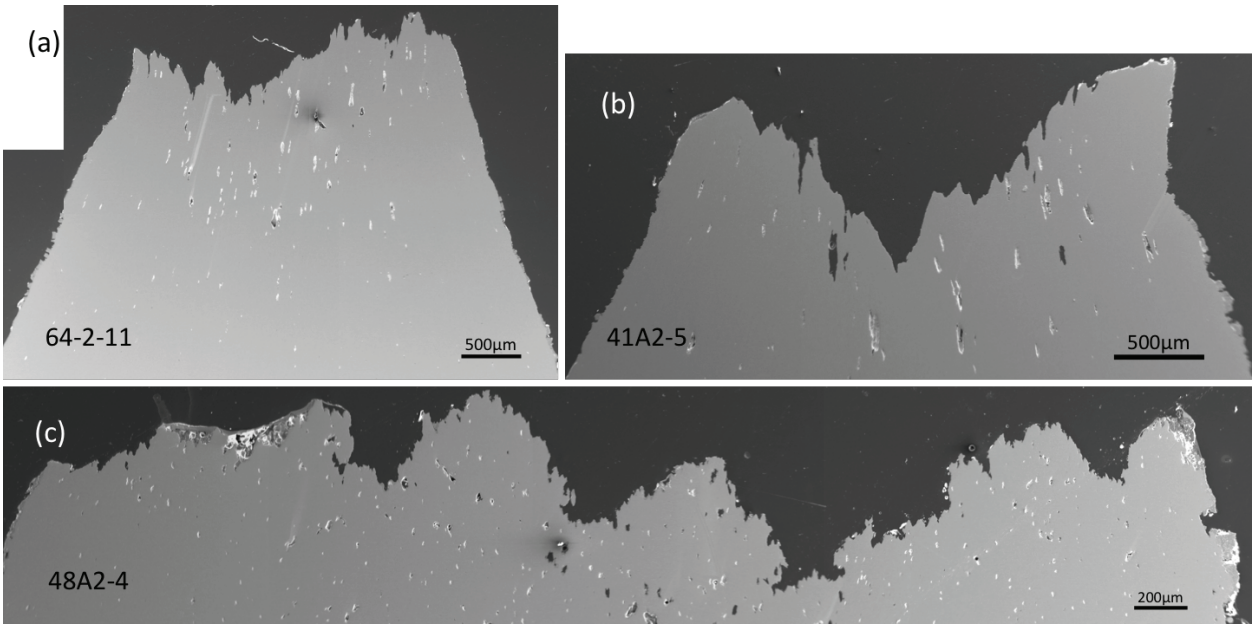

Fig. 7. Secondary electron images of creep-ruptured samples at the necking region of (a) 64-2-11, (b) 41A2-5, and (c) 48A2-4 tested at 650°C and 90 MPa.

Energy dispersive x-ray spectroscopy (EDS) analyses were conducted at the some of the voids in the necking region of 41A2-5 and 48A2-4. To have a better comparison, voids with a similar shape (approximately globular) are presented for 41A2-5 and 48A2-4 in Fig. 8 and Fig. 9, respectively. Fig. 8 shows EDS maps of a void at the necking region of 41A2-5, which show some Cr/W/Si/Mo-rich particles, likely to be $(Cr,Si,W,Mo)_{23}C_6$ and $Fe_2(W,Si,Mo)$ type precipitates in sizes $\leq$~1 µm, surround the void and are also distributed in the further regions, together with a Cr/Mn/V-rich oxide particle in ~2–3 µm at the top of the void. Such big Cr/Mn/V-rich oxide particles were observed in all the samples, retaining intact interface with matrix without associating with any cracks. There is no obvious enrichment inside the void except for minor oxygen enrichment at the edge of the void.

Compared to 41A2-5 in Fig. 8, 48A2-4 in Fig. 9 shows EDS spectra from the "inclusion" (or center) of two voids in the necking region. The void in the "initial" state as shown in Fig. 9a has "inclusion" almost fully filling the void. EDS spectrum in Fig. 9b shows the W/Si/Mo-rich "inclusion", which may suggest a cluster of $Fe_2(W,Si,Mo)$ type Laves phase. In contrast, the void in the "final" state as shown in Fig. 9c only remains a small "inclusion", leaving a large open void. The EDS spectrum in Fig. 9d indicates that the remained inclusion is primarily a Si-rich oxide particle. It's unclear how the "initial" big Laves type cluster was reduced to significantly smaller sizes by oxygen involvement. A possible hypothesis is reacting with oxygen and hydrogen, resulting in the formation of volatile phases such as MoO_3 and $WO_2(OH)_2$, which consumed up Mo and W and left a primarily Si-rich oxide particle.

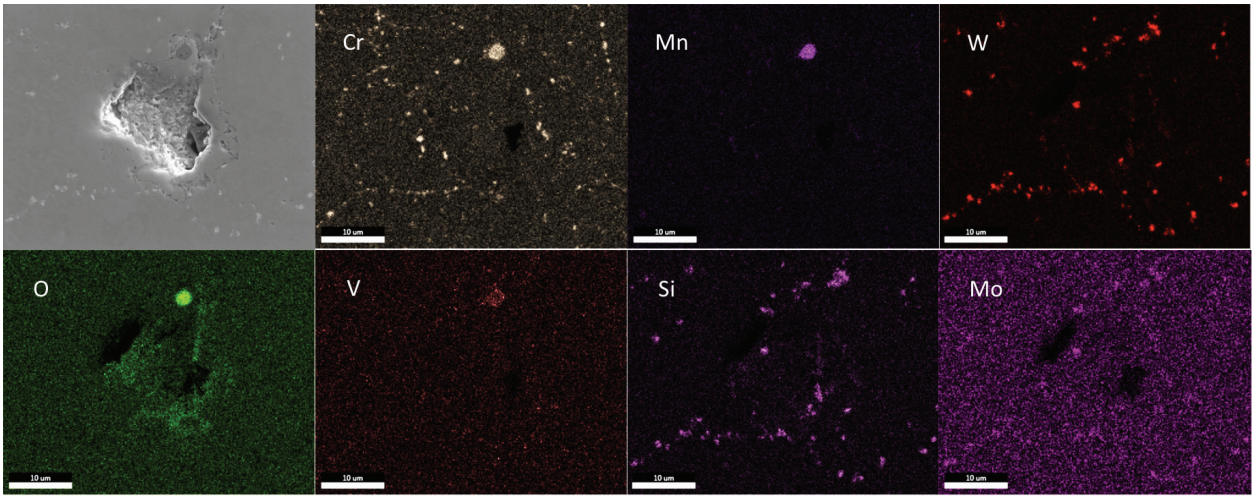

Fig. 8. Secondary electron image and corresponding area EDS maps of a creep void in the necking region of 41A2-5 tested at 650°C and 90 MPa.

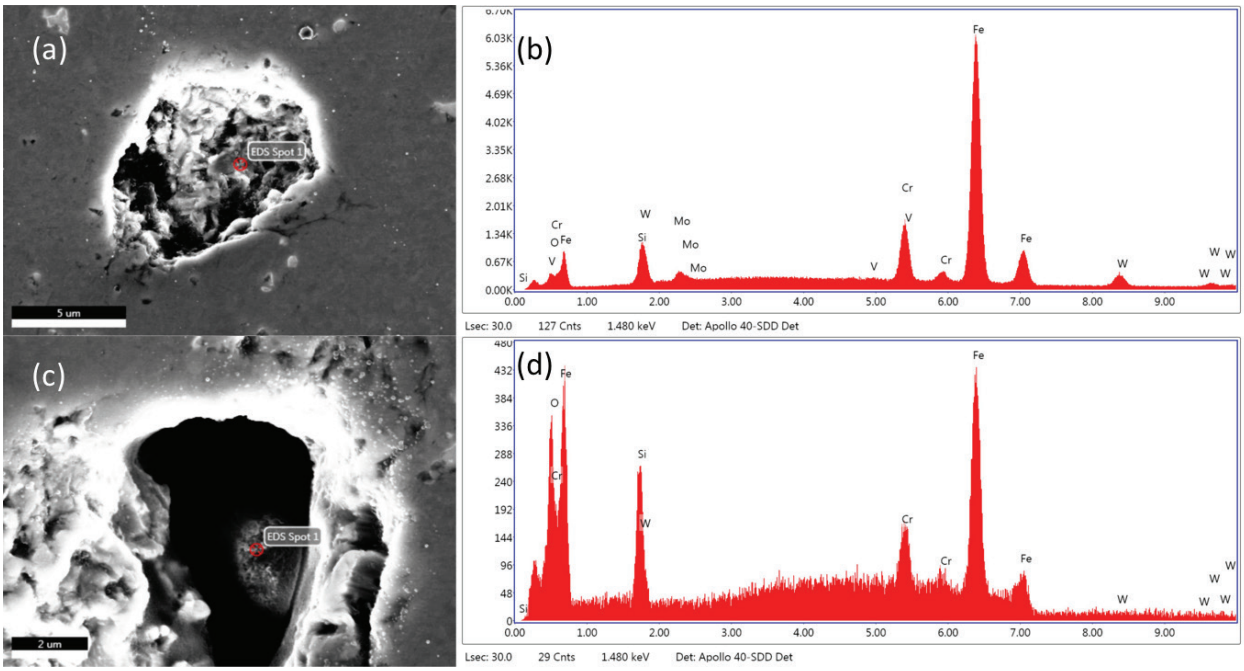

Fig. 9. Secondary electron images and the EDS spectra at the marked locations inside creep voids in the necking region of 48A2-4 tested at 650°C and 90 MPa.

4.3 TEM

Fig. 10a-c shows bright-field STEM images taken under the [011] zone axis from the gauge section of 64-2-11. Fig. 10b indicates that lath structure retained in the gauge section, together with coarse (>~100 nm) dark gray particles at the lath boundaries. The higher magnification image in Fig. 10c shows a few fine (~50 nm) light gray particles (identified to be VN type) as labelled with "p". There are no obvious ultrafine

precipitates in the matrix. However, the diffraction pattern in Fig. 10a shows some secondary reflections in addition to the primary reflections from the matrix in a [011] zone axis. For comparison, the microstructure of the tab section of 64-2-11 is shown in Fig. 10d-g. The bright-field STEM in Fig. 10e shows lath structure, similar to that in the gauge section, which was taken under a [111] zone axis. There are no detectable secondary reflections in the diffraction pattern in Fig. 10d. However, the high-resolution TEM image in Fig. 10f and its fast Fourier transform in Fig. 10g do show some secondary reflections and the correlated disorder features (<1 nm). The secondary reflections under the [111] zone axis (Fig. 10g) as well as that under the [011] zone axis (Fig. 10a) need further investigations to identify their origins either new precipitates formation or just local structure disordering.

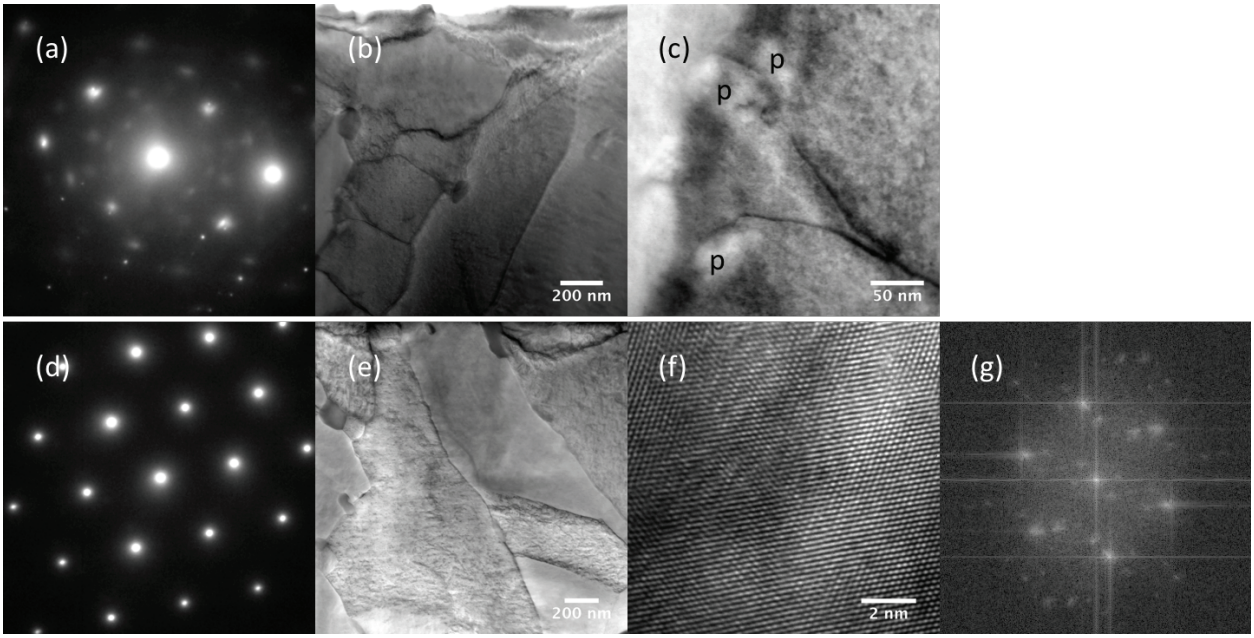

Fig. 10. (b-c) Bright-field STEM images taken under (a) a [011] zone axis at the gauge section and (e) bright-field STEM and (f) high-resolution TEM images taken under (d) a [111] zone axis with (g) fast Fourier transform of (f) at the tab section of 64-2-11 tested at 650°C and 90 MPa.

Fig. 11 shows bright-field STEM images at both the (a-c) gauge and (d-e) tab sections, which were both taken under (f) a [001] zone axis. The gauge section exhibits noticeable grain recovery as shown in Fig. 11a, which is in contrast to the retained lath structure at the tab section as shown in Fig. 11d. Other than grain recovery, dislocations generated from the boundary of coarse precipitates, e.g., Laves phase in Fig. 11b, were often observed at the gauge section, which is similar to that observed at the gauge section of 64-2-11. The more pronounced feature is many ultrafine (~1–6 nm) precipitates exist in both the gauge (Fig. 11c) and tab (Fig. 11e) sections, with the gauge section having generally large sizes of such precipitates. Such ultrafine precipitates excited secondary reflections in addition to the primary reflections from matrix in the [001] zone axis as shown in Fig. 11f, which could be MX (M=metal, X=C/N) type precipitates. Such ultrafine precipitates were not observed in 64-2-11.

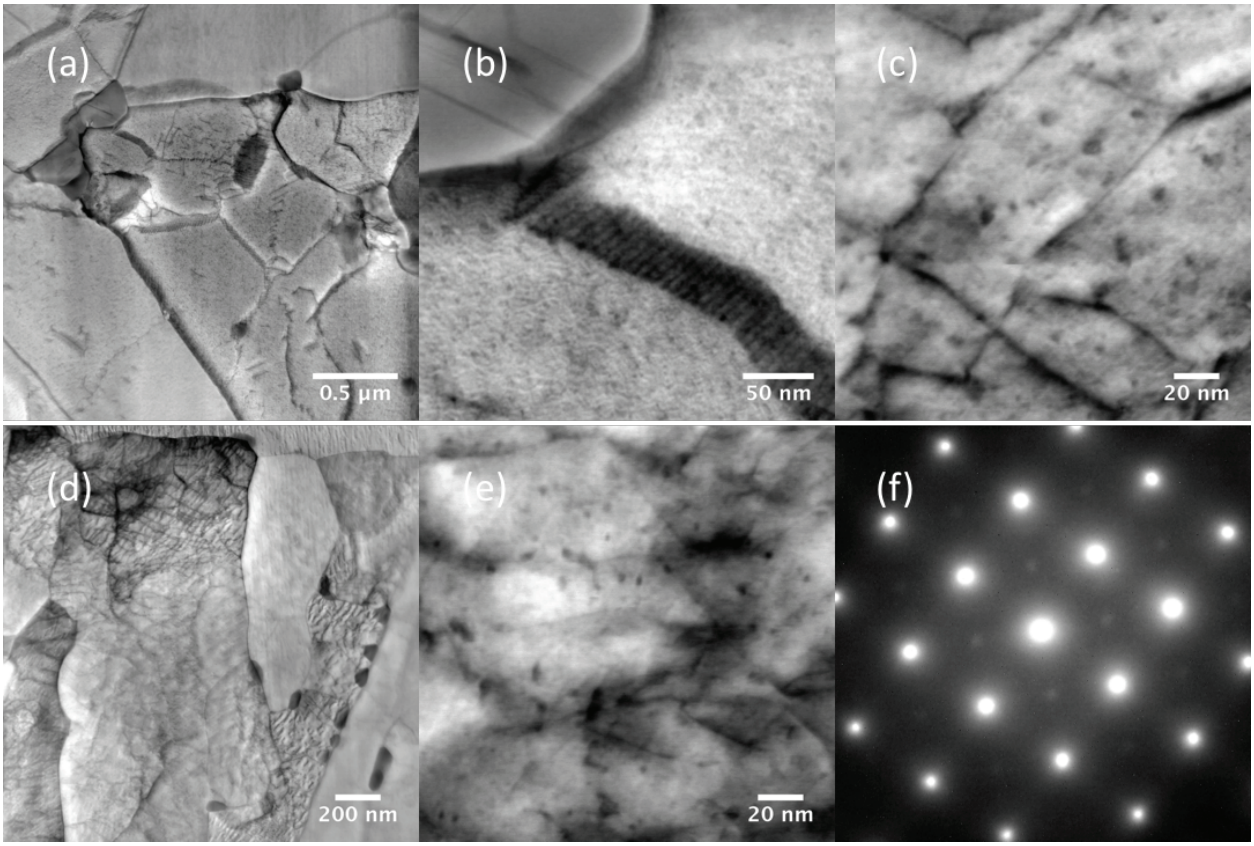

Fig. 11. Bright-field STEM images at the (a-c) gauge and (d-e) tab sections taken under (f) the [001] zone axis of 48A2-4 tested at 650°C and 90 MPa.

5. DISCUSSIONS

5.1 MICROSTRUCTURES

Microstructure difference between the samples with normal (64-2-11 and 41A2-5) and reduced (48A2-4) creep rupture ductility is summarized in Table 6. It is believed that the primary difference between the two scenarios is the formation of high-density ultrafine (~1–6 nm) precipitates in the sample with reduced creep rupture ductility, while the only local disordering (or precipitates) with sizes <1 nm formed in the sample with normal creep rupture ductility.

- The high-density ultrafine precipitates would yield a decent amount of hardening according to the size-dependent strength factor for strength estimation using the dispersed barrier-hardening model [15]. However, such ultrafine precipitates could not effectively pin boundaries to prevent grain recovery. The ultrafine precipitates might also act as trapping sites for voids nucleation and prevent voids coalescence, resulting in the dispersed small globular voids with reduced creep rupture ductility (e.g., 48A2-4). Further experimental investigations are needed to confirm this hypothesis and identify its correlation with EDS-characterized voids with W/Si/Mo-rich cores as shown in Fig. 9.

- In contrast, the local disordering (or precipitates) with sizes <1 nm could not act as an effective strengthening element because of its super-low strength factor or even negative strength factor when the size is smaller than the critical size [15], which would result in either negligible strengthening or minor softening effect. The interfaces between such type of disordered structure and matrix would not be an effective trapping size for void nucleation. Consequently, void coalescence and elongation in the necking region could occur as usual in the samples with normal creep rupture ductility (e.g., 64-2-11 and 41A2-5).

Table 6. Microstructure difference between the samples with normal and reduced creep rupture ductility.

Microstructure		Normal creep rupture ductility		Reduced creep rupture ductility
		64-2-11	41A2-5	48A2-4
Necking		Large, with elongated grains along tensile direction		Small, with little elongated refined grains
Void	Shape	Elongated along tensile direction		Globular
	Size/Denstiy	Large/Low		Small/High
	Chemistry	No obvious enrichment with minor oxygen enrichment at the void boundary		From W/Si/Mo-rich to primarily Si/O-rich
Gauge vs Tab		Retained lath structure, with local disordering (or precipitates) <1 nm		Grain recovery at gauge, with high-density ultrafine precipitates formation (~1–6 nm)

5.2 VICKERS HARDNESS

The Vickers hardness using a 0.1 kgf load was measured at the tab, gauge, and necking regions of the Opt.G92 samples tested at 650°C and 90 MPa, except for the samples of 41A204, 48A2-5, and 48A2-26. The measured hardness as a funciton of time to rupture of the samples are plotted in Fig. 12. The tab region slightly softened after ~2,000 h and stabilized after ~4,000 h. The hardness at the gauge region approximately follows the evolution as that at the tab region. The hardness at the gauge region is generally ~50 HV0.1 lower than that at the tab region. However, the hardness at the necking region gradually decreases with the increasing time to rupture, except for the sample (48A2-4) with reduced creep rupture ductility showing a sudden

hardness drop accompanied with some hardness increases at the gauge and tabe regions. As discussed above, the high-density of ultrafine precipitates in 48A2-4 would act as a strengthening element for the increased hardness at the gauge and tab regions. However, the dispersed small voids in the necking region of 48A2-4 might have signficantly reduced the hardness with the greatest standard deviation because of the low-load-induced small indents. In comparison, the samples with normal creep rupture ductility (e.g., 64-2-11 and 41A2-5) do not show remarkable hardness changes at the tab, gauge, and necking regions, which confirm that the local disordering (or precipitates) with sizes <1 nm does not noticeably influence the hardness.

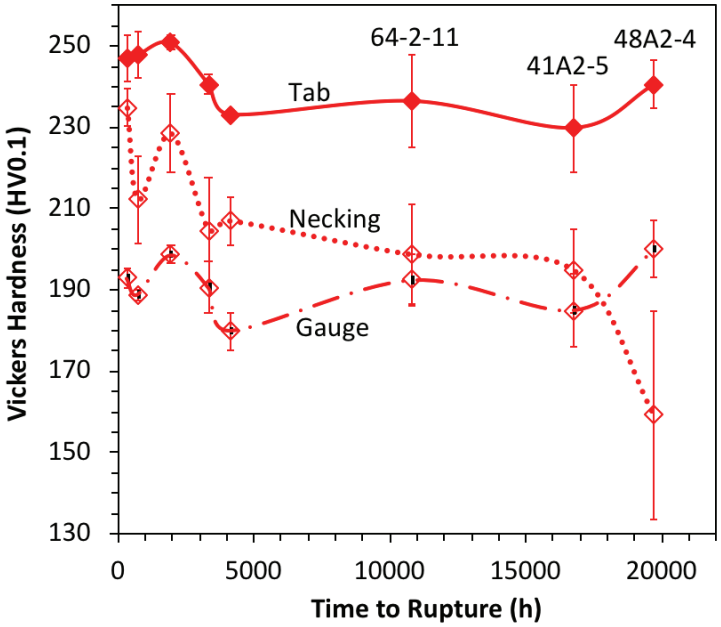

Fig. 12. Vickers hardness (HV0.1) at the tab, gauge, and necking regions of the Opt.G92 samples tested at 650°C (excluding the samples of 41A2-4, 48A2-5 and 48A2-26).

5.3 HEATS CHEMISTRY

Recent analyses on creep rupture ductility of Grade 91 suggested the close relationship between heat chemistry and low creep rupture ductility. After a detailed review of the large creep rupture database, Electric Power Research Institute (EPRI) proposed a tight chemistry for P91, named as Class 2, during the ASME Boiler Code Week meeting in August 2015. Compared to the specified chemistry of P91 in ASTM A335–11, "Standard specification for seamless ferritic alloy-steel pipe for high-temperature service", the maximum limits for Mn, Ni, Si, P, and S contents are reduced in P91 Class 2, together with the newly added limits for tramp elements such as Cu (≤0.10), W (≤0.010), B (≤0.001), As (≤0.010), Sn (≤0.010), Sb (≤0.003), and Pb (≤0.001) in weight percent (wt%). Heats with chemistry complying with the proposed P91 Class 2 showed satisfactory creep rupture ductility.

Following the Grade 91 heat chemistry analysis, Grade 92 also showed the effect of heat chemistry on creep rupture ductility despite the smaller database of Grade 92 compared with that of Grade 91. The heat, having noticeably higher contents of Ni and S, showed low creep rupture ductility at 600 and 650°C ("+" signs in Fig. 4) [12]. Tramp elements such as Cu, As, Sn, Sb, Pb, O, etc. were not reported in the heats chemistry, some of which might have high contents of the tramp elements detrimental to creep rupture ductility. For example, all heats of Grade 91 Tenaris products were found to have Cu content ≤ 0.20%, but about 85% of the Grade 91 products have Cu content ≥ 0.10%. Therefore, detailed chemistry analyses were conducted on #41A2 (normal creep rupture ductility) and #48A2 (reduced creep rupture ductility).

Fig. 13 shows the analyzed chemsitry of #41A2 and #48A2 by using IGF (inert gas fusion) for O and N, combustion for C and S, ICP-MS (inductively coupled plasma-mass spectroscopy) for As, Bi, P, Pb, Sb, and Sn, and ICP-OES (inductively coupled plasma- optical emission spectroscopy) for the other elements. It is clear that #48A2 has higher content of tramp elements of Al, Ca, Ti, Y, and Zr although their content is less than 0.01 wt% or 0.001 wt%. These tramp elements tend to form oxides, nitrides, or complex inclusions, detrimental to creep rupture ductility.

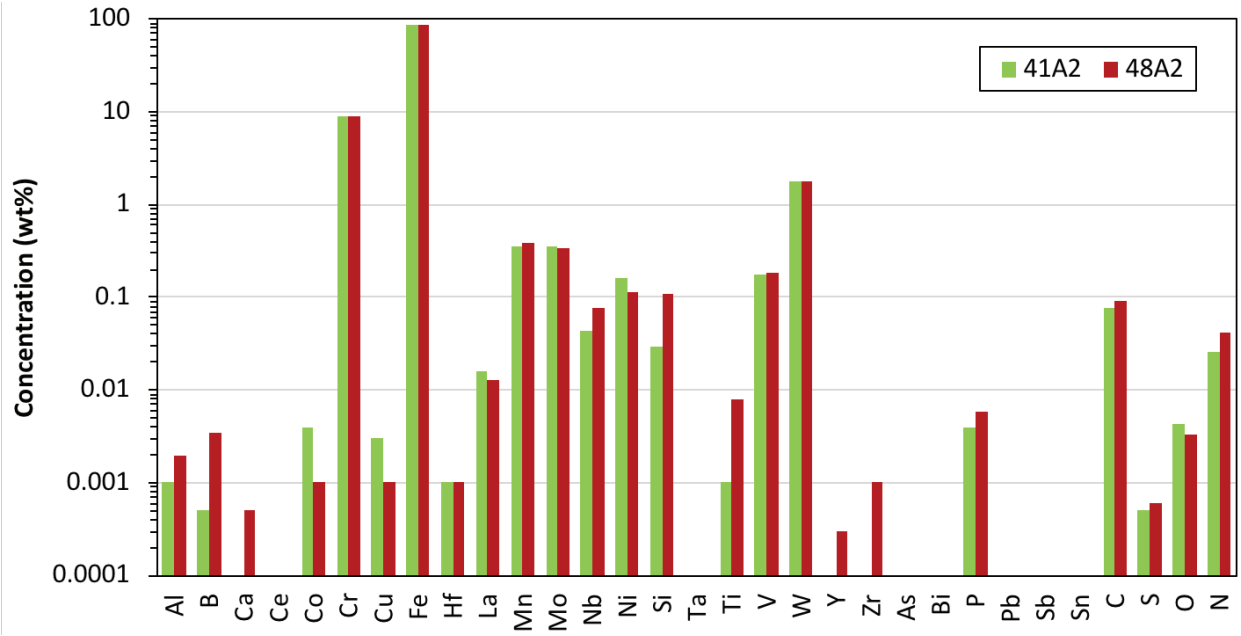

Fig. 13. Analyzed compositions of #41A2 and #48A2. The elements without bars indicate their lower concentration of Ca/Y < 0.0003, Ce/Ta/Zr < 0.001, and As/Bi/Pb/Sb/Sn < 0.0001.

To better understand the heat chemistry, GD-OES (glow discharge-optical emission spectroscopy) was employed to re-analyze the #41A2 and #48A2. Fig. 14 shows the GD-OES results of (a-b) #41A2 and (c-d) #48A2, which plots the intensity of each element because of the lack of standards for many of the tramp elements. Higher intensities correspond to higher concentration in general. Other than the distinction revealed in Fig. 13, the GD-OES results indicate that #48A2 has a higher tramp element content of Ag, Pb, Hf, H, and D compared to #41A2. Among the higher content of tramp elements, the H and D content in #48A2 is significantly higher than that in #41A2, which may correlate with Fig. 9b of 48A2-4 showing disappeared W by forming volatile $WO_2(OH)_2$.

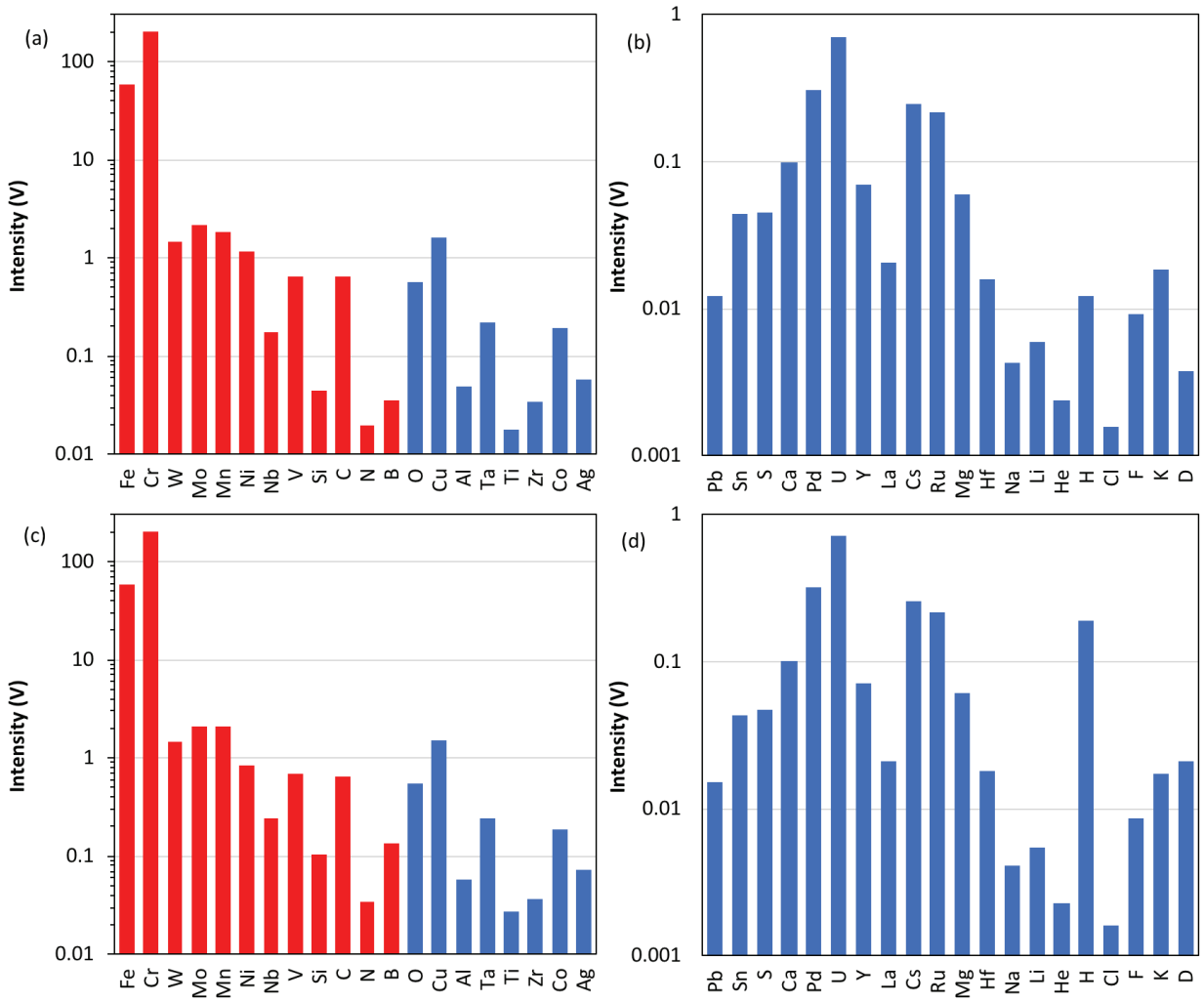

Fig. 14. GD-OES analyzed intensity of the elements in (a-b) #41A2 and (c-d) #48A2, with red and blue for the alloying and tramp elements, respectively.

6. SUMMARY

This report presents the up-to-date intermediate-term creep rupture test results of Opt.G92, which include samples primarily from the as-received TMT condition and one sample in the re-normalized and tempered (Re-N&T) condition. The tests were conducted at 550, 600, and 650°C in air with stresses ranging from 90 to 280 MPa. A total of 21 samples were tested at ORNL and 4 samples at INL. Among the ORNL samples, three of them are still running, with the longest test time >39,863 h at 550°C.

In general, the creep-ruptured samples exhibited consistently superior creep resistance, in terms of longer time to rupture, higher creep strength, and lower minimum creep rate, compared to Grades 92 and 91. For example, Opt.G92 with TMT increased creep strength by ~50 and ~60 MPa with minimum creep rate about two orders of magnitude lower than P92 and P91, respectively, at 550°C. The ongoing test of the Opt.G92 sample in the Re-N&T condition also showed significant enhancement in creep resistance. Although the enhancement in creep resistance of Opt.G92 over P92 and P91 became smaller at higher temperatures, the enhancement is still noticeable at 650°C. Detailed creep resistance advantages of Opt.G92 over P92 and P91 are summarized in Table 4.

Creep rupture ductility analysis of the available databases of Grades 92 and 91 indicated that creep at higher temperatures tends to have low creep rupture ductility (e.g., reduction of area). Grade 92 data showed consistent trends in the relationships between rupture ductility and stress or time to rupture at 550, 600, and 650°C with T92 generally having lower creep rupture ductility than P92. Following the trends, Grade 92 is not expected to have reduction of area ≤20% at 550°C unless the stress is <~160 MPa with time to rupture >1,000 kh (or >~114 years), which is way beyond the service life of a nuclear reactor. In contrast, the relationship between rupture ductility and stress or time to rupture of Grade 91 with a larger database is not consistent at the test temperatures. However, Grade 91 generally has greater resistance to low creep rupture ductility than Grade 92, in terms of the need of lower stress or longer time to rupture to trigger low creep rupture ductility. Compared to Grade 92 initiated reduction of creep rupture ductility with reduction of area ≤70% at stresses <~100 MPa (or time to rupture >~3 kh) and exhibited low creep rupture ductility with reduction of area ≤20% at stresses <~90 MPa (or time to rupture >~10 kh) at 650°C, Opt.G92 with TMT did not show the initiation of reduction of creep rupture ductility after 16,769.3 h at 650°C and 90 MPa, except for three samples from a VIM-only heat exhibited reduced creep rupture ductility to 30.8–38% reduction of area. The creep rupture ductility comparison between Opt.G92 and Grades 92 and 91 is summarized in Table 5.

To understand the reason for the normal creep rupture ductility of the samples from the VIM+ESR heats compared to the reduced creep rupture ductility of the samples from the VIM-only heat, microstructural characterization, Vickers hardness measurement, and heat chemistry analysis were conducted. As summarized in Table 6, the sample (48A2-4) from the VIM-only heat (#48A2) had reduced creep rupture ductility, associated with dispersed small globular voids in the fracture end with small necking, while the samples (64-2-11 and 41A2-5) from the VIM+ESR heats (#64-2 and #41A2) had normal creep rupture ductility, associated with large voids elongated along tensile direction within the large necking region. Two hypotheses are proposed to answer the distinct creep rupture ductility behavior between the VIM-only and VIM+ESR heats:

- High-density ultrafine precipitates (~1–6 nm) formed in the VIM-only heat during creep acted as trapping sites for void nucleation and prevented void coalescence, resulting in the dispersed small globular voids. In the meantime, the ultrafine precipitates hardened the material as confirmed by Vickers hardness measurement, which tended to embrittle the material. In contrast, only local disordering (or precipitates) with sizes <1 nm was formed in the VIM+ESR

heat during creep, which could not be effective void nucleation sites and barriers for subsequent voids coalescence, as well as not able to harden the material.

- Chemistry analyses by a variety of techniques indicated the higher content of tramp elements (e.g., Al, Ca, Ti, Y, Zr, Ag, Pb, Hf, H and D) in the VIM-only heat compared to that in the VIM+ESR heat. The content of H and D was significantly higher in the VIM-only heat, which might have favored volatile phases formation, e.g., $WO_2(OH)_2$, because of oxygen involvement for air in the necking region of the test sample.

Further experimental investigations are needed to confirm and clarify the two hypotheses to understand the overall superior creep resistance, including both creep strength and creep rupture ductility, of VIM+ESR heats of Opt.G92. In summary, Opt.G92 in VIM+ESR heats exhibited significant enhancement in creep resistance with normal creep rupture ductility compared to Grades 92 and 91. Well chemistry and microstructure control can yield excellent performance.

REFERENCES

[1] J.T. Busby, *Advanced Structural Materials Development for Advanced Fast Reactor Systems: 2009 Strategic Plan*, ORNL/TM-2009/199.

[2] J.T. Busby, T.S. Byun, R. Klueh, P. Maziasz, J. Vitek, K. Natesan, M. Li, R. Wright, S. Maloy, M. Toloczko, A. Motta, B.D. Wirth, G. R. Odette, and T. Allen, *Candidate Developmental Alloys for Improved Structural Materials for Advanced Fast Reactors*, ORNL/TM-2008/040.

[3] L. Tan, P.J. Maziasz, T.-L. Sham, *Report on the Optimization and Testing Results of Advanced Ferritic/Martensitic Alloys*, ORNL/TM-2012/288.

[4] L. Tan, M.A. Sokolov, T.-L. Sham, *Report on FY15 property assessments of optimized Grade 92 with TMT*, ORNL/TM-2015/291.

[5] L. Tan, *FY16 property assessments of optimized Grade 92 with TMT*, ORNL/TM-2016/326.

[6] L. Tan, Y. Yamamoto, T.-L. Sham, *Materials Procurement and Related Examinations of Advanced Ferritic-Martensitic and Austenitic Alloys*, ORNL/TM-2013/325.

[7] L. Tan, Y. Yamamoto, T.-L. Sham, *FY14 Materials Procurements and Related Examinations of Optimized Grade 92 and Alloy 709 Steels*, ORNL/TM-2014/258.

[8] NIMS Creep Data Sheet No. 48A

[9] NIMS Creep Data Sheet No. 43A

[10] J. Hald, *Creep strength and ductility of 9 to 12% chromium steels*, Materials at High Temperatures 21 (2004) 41-46.

[11] E.I. Samuel, B.K. Choudhary, D.P.R. Palaparti, M.D. Mathew, *Creep deformation and rupture behaviour of P92 steel at 923 K*, Procedia Engineering 55 (2013) 64–69.

[12] Y. Gu, G.D. West, R.C. Thomson, J. Parker, *Investigation of creep damage and cavitation mechanisms in P92 steels*, in: D. Gandy, J. Shingledecker (Eds.), Advances in Materials Technology for Fossil Power Plants, Proceedings from the Seventh International Conference, October 22–25, 2013, Waikoloa, Hawaii, USA, pp. 596–606.

[13] C. Panait, A.-F. Gourgues-Lorenzon, J. Besson, A. Fuchsmann, W. Bendick, J. Gabrel, M. Piette, *Long-term aging effect on the creep strength of the T92 steel*, 9th Liege Confer: Materials for Advanced Power Engineering, Liege, Belgium 2010.

[14] R.W. Swindeman, M.J. Swindeman, B.W. Roberts, B.E. Thurgood, D.L. Marriott, *Verification of allowable stresses in ASME Section III subsection NH for Grade 91 steel*, ASME Standards Technology, LLC, STP-NU-019-1, 2009.

[15] L. Tan, J.T. Busby, *Formulating the strength factor α for improved predictability of radiation hardening*, J. Nucl. Mater. 465 (2015) 724–730.